Effect of flow pulsation on mass transport in a cathode channel of polymer electrolyte membrane fuel cell

Hun Sik Han [a], Yun Ho Kim [b], Seo Young Kim [c,*], Jae Min Hyun [a]

[a] Division of Mechanical Engineering, Korea Advanced Institute of Science and Technology, 291 Daehak-ro, Yuseong-gu, Daejeon 305-701, South Korea
[b] Air-Conditioning R&D Laboratory, LG Electronics, 327-23 Gasan-dong, Geumcheon-gu, Seoul 153-802, South Korea
[c] Energy Mechanics Research Center, Korea Institute of Science and Technology, P.O. Box 131, Cheongryang, Seoul 130-650, South Korea

ABSTRACT

An experimental and theoretical study on the cathode flow pulsation in a polymer electrolyte membrane (PEM) fuel cell is performed. A 10-cell PEM fuel cell stack with open-air cathode channels is employed to investigate the effects of the cathode flow pulsation on the overall performance. The polarization and corresponding power curves obtained show that both the limiting current density and the maximum power density are substantially enhanced when the pulsating component is added to the cathode mainstream flow. The flow pulsation at $Re = 77$ provides the maximum increment of 40% and 35.5% in the limiting current density and in the maximum power density, respectively. The enhancement of the overall performance is more pronounced at low Reynolds numbers. Also, the theoretical mass transport analysis in the pulsating cathode flow channel is carried out to verify the present experimental results. The momentum and species conservation equations are analytically solved, and the effective time-averaged dispersion coefficient is defined to account for the enhanced mass transport by the flow pulsation. Comprehensive analytical solutions show that the effect of the relevant parameters is in well accordance with the experimental results.

© 2012 Elsevier B.V. All rights reserved.

1. Introduction

As a new and environment-friendly energy source, fuel cells have been a subject of intense research interest due to their high energy efficiency, low emission, few moving parts, low noise and cleanness of energy production, to name a few. The fundamental aspects of fuel cells have been well documented in [1–3]. Among various types of fuel cells, a polymer electrolyte membrane (PEM) fuel cell is expected as one of the most promising candidates for future power source on account of its high power density, simple structure, quick start-up and easy operation [4].

A practical PEM fuel cell system consists of a fuel cell stack and a balance-of-plant (BOP) system for the stack operation such as a fuel supply subsystem, an air supply subsystem, a water management subsystem, a thermal management subsystem and a power electronics subsystem [1]. In the air supply subsystem, a blower or a compressor is generally used to feed air to the cathode channel of a stack. As the supplied air travels along the channel, oxygen is simultaneously being consumed by the electrochemical

reaction. The oxygen concentration at the wall catalyst layer is lower than that in the core cathode flow channel due to the electric current harvested at the wall reaction site. The fuel cell performance is strongly affected by the diffusive mass transport through the electrode layer which is proportional to the reactant concentration gradient between the catalyst layer in the membrane-electrode assembly (MEA) and the flow channel in the bipolar plate.

As the current generated from the cell increases, the higher electrochemical reaction rate is required. Therefore, the reactant concentration at the reaction site decreases since the reactant is rapidly consumed to meet the increased current output. The mass transport limit is reached when the reactant concentration at the catalyst layer drops to zero [1,2]. Such a mass transport limit determines the limiting current density j_L which is the maximum current output from the cell. Fuel cells cannot operate beyond j_L, at which the reversible cell voltage is entirely canceled out by the concentration loss. In the fuel cell mass transport design, therefore, the focus is on increasing j_L which is determined by the maximum reactant transport rate.

To extend j_L, it is important to maintain the reactant concentration in the flow channel as high as possible. Thus, high-powered blowers for enhanced reactant feeding are adopted in practical PEM fuel cell systems. However, the increase of blowing capacity brings

Nomenclature

a	pulsating amplitude (m)
A	dimensionless pulsating amplitude
Ar	aspect ratio
b	half of cathode channel width (m)
c	oxygen concentration (mol m^{-3})
C	dimensionless oxygen concentration
D_e	effective time-averaged dispersion coefficient (m^2 s^{-1})
D_m	oxygen molecular diffusivity (m^2 s^{-1})
E_D	dispersion coefficient ratio
E_j	limiting current density enhancement factor
E_P	maximum power density enhancement factor
E_σ	wall shear stress ratio
f	pulsating frequency (Hz)
F	Faraday constant (96,485.34 C mol^{-1})
H	cathode channel height (m)
j	current density (A cm^{-2})
j_L	limiting current density (A cm^{-2})
k_0	pressure gradient in steady flow (kg m^{-2} s^{-2})
k_1	amplitude of pressure fluctuation (kg m^{-2} s^{-2})
l	channel length occupied by MEA (m)
L	cathode channel length (m)
n	number of mole electrons per mole reactant
$\dot{N}''$	axial mass flux (mol m^{-2} s^{-1})
p	total pressure (kg m^{-1} s^{-2})
P	power density (W cm^{-2})
q_w	oxygen mass flux at a permeable side wall (mol m^{-2} s^{-1})
Re	Reynolds number
S	interaction function between velocity and concentration profiles

Sc	Schmidt number
t	time (s)
u	velocity in x direction (m s^{-1})
U	dimensionless velocity in X direction
V	voltage (V)
W	cathode channel width (m)
Wo	Womersley number
x, y	axial and transverse coordinates (m)
X, Y	dimensionless axial and transverse coordinates

Subscripts and superscripts

avg	average
b	bulk state
cell	fuel cell
in	channel inlet
max	maximum
out	channel outlet
st	standard condition, 273 K and 1 atm
stack	fuel cell stack
0	steady component
1	unsteady component

Greek symbols

ε	amplitude of velocity fluctuation
η	efficiency
μ	fuel utilization coefficient
ν	kinematic viscosity (m^2 s^{-1})
ρ	fluid density (kg m^{-3})
σ	wall shear stress (kg m^{-1} s^{-2})
τ	dimensionless time
ω	angular velocity of pulsating flow (s^{-1})

forth the excessive parasitic power loss and increased system volume, weight and noise level. For this reason, a new mass transport enhancing scheme has been suggested to reduce high reactant stoichiometry [5], and they demonstrated that the fuel cell performance could be enhanced by the reactant pulsating supply which enhanced axial dispersion of the reactant.

This paper intends to address the impact of the cathode flow pulsation on the PEM fuel cell performance. The polarization and corresponding power curves are experimentally obtained to identify the influence of the Womersley number and the Reynolds number in the cathode flow channel on the overall performance of a 10-cell PEM fuel cell stack. The fuel cell performance in the case of a pulsating cathode flow is compared with that in the steady non-pulsating flow in terms of the maximum power density and the limiting current density. In addition, a theoretical mass transport analysis for the pulsating cathode flow is conducted to verify the present experimental results for PEM fuel cell stack.

2. Experimental setup and procedure

The experimental setup was composed of an air supply, a hydrogen supply, a nitrogen supply, a temperature control unit and a PEM fuel cell stack, as shown in Fig. 1. An NP50 PEM fuel cell stack (heliocentric Energiesysteme GmbH) with 10 cells was employed. The active area of a cell was 5 cm × 5 cm and each cell had 14 parallel and straight open-air cathode channels of 1.93 mm (H) × 3.0 mm (W) × 70 mm (L) as sketched in Fig. 2.

Compressed hydrogen of 99.999% purity was supplied to the anode, which was controlled by an MFC. Air was fed to the cathode channels from a compressed air tank through a rectangular Plexi-glas duct of 60 mm in width, 56 mm in height and 870 mm in length, where a pulsating component was added by a woofer. Three-stage mesh screens and a honeycomb were installed to produce a uniform inlet flow with low turbulence intensity of 0.68% for the steady flow at $Re = 135$. The flow rate, temperature and humidity were controlled by an MFC, a heater and a humidifier, respectively.

An acoustic woofer (Sammi Sound Technology Corporation, SR-08B100) was installed in a rectangular chamber to produce an oscillatory flow. The rectangular chamber for the woofer was connected to the Plexiglas duct with a flexible tube to eliminate transmission of structural vibration. A function generator (HP-34401A) produced a sinusoidal signal with a specific frequency and the signal was amplified by a signal amplifier (Inkel, AX7030G). The function generator and the signal amplifier consumed the electric power up to 23 W and 35 W, respectively. The amplified signal was delivered to the woofer via a digital oscilloscope (LeCroy, LT342) to check the input frequency and voltage. The time-variant pulsating velocity was measured at the mid portion of the cathode channel inlet by a hot-wire anemometry (Dantec Streamline® System) to determine the amplitude and frequency of the pulsating flow and the time-averaged flow velocity. After reaching a time-periodic quasi steady-state, the experimental data were stored in a data acquisition device (Yokogawa, DS 400) for analysis.

In an effort to get consistent experimental data, the following procedure was adopted during the start-up, performance measurement and shutdown of stack operation [5,6]. At the beginning of the experiment, nitrogen was fed to the stack for 20 min to purge impurities inside the anode and cathode channels.
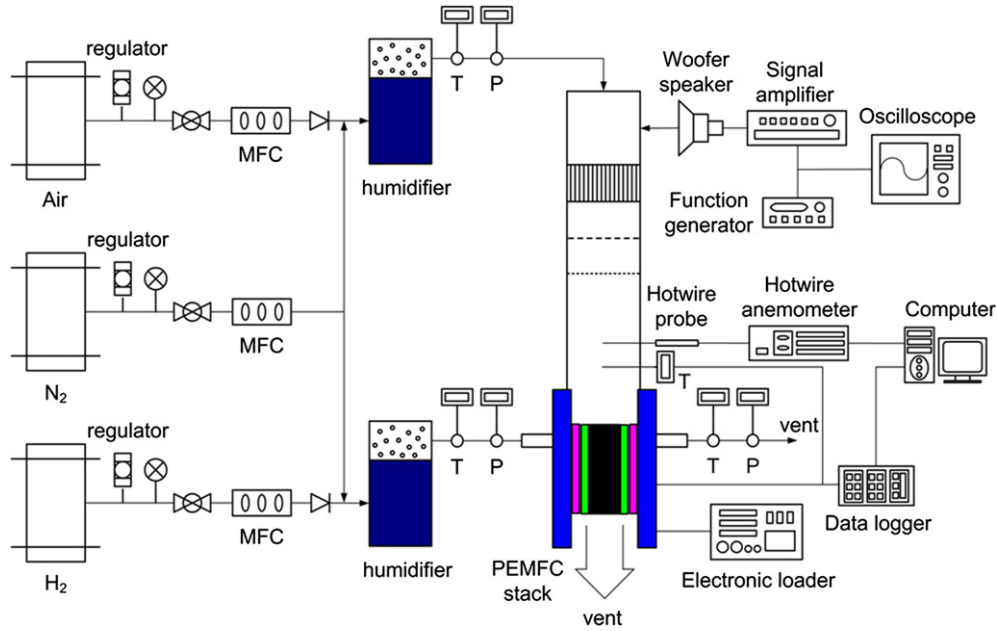
Fig. 1. Schematic diagram of the experimental setup.

Then, air and hydrogen were supplied for 30 min under a current loading of 3 A to activate the MEA inside the stack. After reaching a steady-state, the open-circuit-voltage was measured. The current loading was increased to a specific value by using an electronic loader (Daegil Electronics Co., EL-500P). The voltage output was determined again from the stack in the steady-state based on the galvanostatic techniques [1]. The polarization curves were finally obtained for various current loading conditions. After finishing the measurement, the external loading was removed and the air and hydrogen supplies were shut off. Then the stack was purged with nitrogen again to prevent degradation of MEA performance due to crossover of hydrogen and oxygen remaining at the anode and cathode channels.
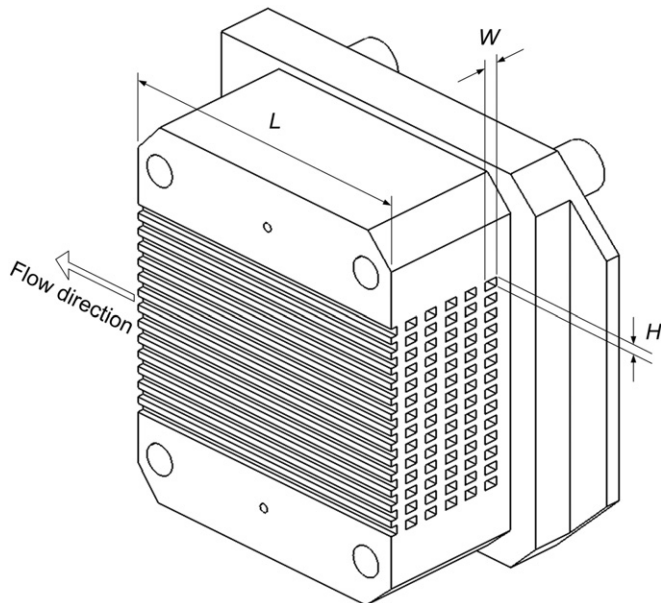

Fig. 2. Configuration of the cathode channels.

3. Theoretical analysis

3.1. Mathematical formulation

Consider a cathode channel (width $2b$ and length l) with a mass permeable side wall, as sketched in Fig. 3. The governing equations for a one-dimensional, unsteady, fully developed, laminar flow of an incompressible fluid, are as follows [7,8]

$$\frac{\partial u}{\partial t} = -\frac{1}{\rho}\frac{\partial p}{\partial x} + \nu\frac{\partial^2 u}{\partial y^2}, \tag{1}$$

$$\frac{\partial c}{\partial t} + u\frac{\partial c}{\partial x} = D_m\frac{\partial^2 c}{\partial y^2}, \tag{2}$$

where $u(y,t)$ represents the fluid velocity in the x direction and $c(x,y,t)$ denotes the oxygen concentration in the cathode channel. The flow pulsation is driven by a sinusoidal pressure pulse, namely [8–15]

$$-\frac{\partial p}{\partial x} = k_0 + k_1\left[e^{i\omega t}\right]_R, \tag{3}$$

where k_0 is the pressure gradient in steady flow, k_1 is the amplitude of the pressure fluctuation, i denotes $\sqrt{-1}$ and the subscript R refers to the real part of the terms shown. To evaluate k_1, it is assumed that the propagation of the pulse wave in the channel follows the same mechanism as the propagation of a sinusoidal pressure wave in a fluid, namely [9,10]

$$k_1 = \omega^2\rho a, \tag{4}$$

where ω is the angular velocity of the pulsating flow, a is the pulsating amplitude, and ρ is the fluid density. The associated boundary conditions are expressed as [1,2,8,11–13]

$$\left.\frac{\partial u}{\partial y}\right|_{y=0}=0,\ u|_{y=\pm b}=0,\ \left.\frac{\partial c}{\partial y}\right|_{y=b}=0,\ D_m\left.\frac{\partial c}{\partial y}\right|_{y=-b}=q_w,\ c_{0b}|_{x=0}=c_{in}. \tag{5}$$

Then, Eqs. (1)–(5) are non-dimensionalized in the following fashion [10–12]
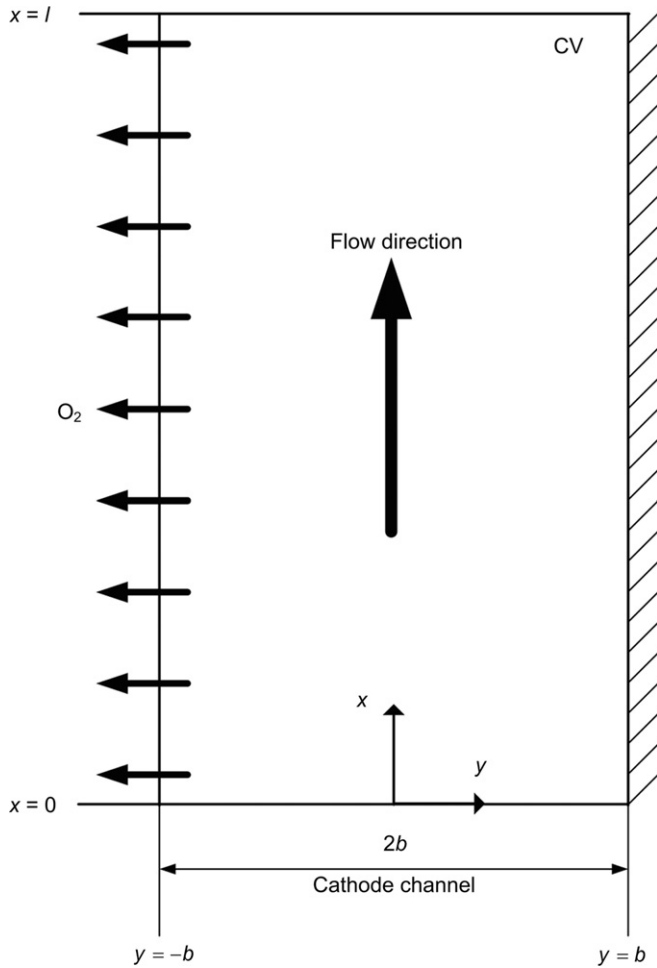
Fig. 3. Control volume for a pulsating cathode channel flow.

$$U = \frac{u}{u_{0\text{avg}}}, \quad X = \frac{D_m x}{u_{0\text{avg}} b^2}, \quad Y = \frac{y}{b}, \quad \tau = \omega t, \quad C = \frac{c - c_{\text{in}}}{q_w b / D_m},$$

$$Wo = b\left(\frac{\omega}{\nu}\right)^{1/2}, \quad Re = \frac{2u_{0\text{avg}} b}{\nu}, \quad Sc = \frac{\nu}{D_m}, \quad A = \frac{a}{b}, \quad (6)$$

where Wo, Re, Sc and A are the Womersley number, the Reynolds number, the Schmidt number and the dimensionless pulsating amplitude, respectively. The Womersley number is the non-dimensional oscillating frequency of the cathode inlet flow. The Reynolds number denotes the non-dimensional and time-averaged air flow velocity and the Schmidt number represents the relative magnitudes of molecular momentum diffusion and mass diffusion in the flow. Here, $u_{0\text{avg}} = (1/b)\int_0^b u_0 \, dy = (k_0 b^2)/(3\rho\nu)$ is the cross-sectional average velocity in a steady flow, and D_m is the bulk oxygen molecular diffusivity.

The governing equations and the associated boundary conditions, in properly non-dimensionalized form, are

$$\frac{\partial U}{\partial \tau} = \frac{3}{Wo^2} + \frac{2Wo^2 A}{Re}\left[e^{i\tau}\right]_R + \frac{1}{Wo^2}\frac{\partial^2 U}{\partial Y^2}, \quad (7)$$

$$\frac{\partial C}{\partial \tau} + \frac{1}{Wo^2 Sc} U \frac{\partial C}{\partial X} = \frac{1}{Wo^2 Sc}\frac{\partial^2 C}{\partial Y^2}, \quad (8)$$

$$\left.\frac{\partial U}{\partial Y}\right|_{Y=0} = 0, \ U|_{Y=\pm 1} = 0, \ \left.\frac{\partial C}{\partial Y}\right|_{Y=1} = 0, \ \left.\frac{\partial C}{\partial Y}\right|_{Y=-1} = 1, \ C_{0b}|_{X=0} = 0, \quad (9)$$

where C_{0b} is the bulk concentration in steady flow defined as $C_{0b} =$

$$\int_{-1}^{1} U_0 C_0 \, dY / \int_{-1}^{1} U_0 \, dY \ [11–13].$$

3.2. Mass transport analysis

Assuming that both the dimensionless velocity U and the dimensionless concentration C consist of a steady component and an imposed unsteady component [11–13], i.e.,

$$U(Y, \tau) = U_0(Y) + U_1(Y, \tau), \quad (10)$$

$$C(X, Y, \tau) = C_0(X, Y) + C_1(Y, \tau), \quad (11)$$

and substituting Eqs. (10) and (11) into Eqs. (7)–(9), the analytic solutions for the velocity and the concentration can be obtained

$$U_0(Y) = -\frac{3}{2}\left(Y^2 - 1\right), \quad (12)$$

$$U_1(Y, \tau) = \frac{2Wo^2 A}{Re}\left[Be^{i\tau}\right]_R, \quad (13)$$

$$C_0(X, Y) = -\frac{X}{2} + \frac{Y^4}{16} - \frac{3Y^2}{8} + \frac{Y}{2} + \frac{39}{560}, \quad (14)$$

$$C_1(Y, \tau) = \frac{A}{Re}\left[Ge^{i\tau}\right]_R, \quad (15)$$

where

$$B(Y) = \frac{1}{i}\left[1 - \frac{\cosh(i^{1/2} Wo Y)}{\cosh(i^{1/2} Wo)}\right]. \quad (16)$$

$$G(Y) = \frac{\tanh(i^{1/2} Wo)\cosh(i^{1/2} Wo Sc^{1/2} Y)}{(1 - Sc)Sc^{1/2}\sinh(i^{1/2} Wo Sc^{1/2})}$$
$$- \frac{\cosh(i^{1/2} Wo Y)}{(1 - Sc)\cosh(i^{1/2} Wo)} - \frac{1}{Sc}. \quad (17)$$

Now, it is possible to calculate the enhanced mass transport in the pulsating flow channel from the velocity and concentration profiles obtained. The effective time-averaged dispersion coefficient D_e can be determined as follows [14,15]

$$-D_e \frac{\partial c}{\partial x} + \frac{1}{2b}\int_{-b}^{b} u_0(y) c_0(x, y) \, dy$$

$$= -D_m \frac{\partial c}{\partial x} + \frac{\omega}{2\pi}\int_0^{2\pi/\omega} \frac{1}{2b}\int_{-b}^{b} u(y, t) c(x, y, t) dy \, dt. \quad (18)$$

The left-hand side of Eq. (18) denotes the effective diffusion flux by the flow oscillation plus the mass flux by the mean flow, and the right-hand side represents the molecular diffusion flux plus the time-averaged convective mass flux produced by the interaction of the cross-stream-varying velocity and concentration profiles. Substituting Eqs. (10)–(15) into Eq. (18) and conducting the time-integration yields the dispersion coefficient ratio which indicates

a measure of the effective time-averaged dispersion coefficient by flow pulsation in comparison to the bulk molecular diffusivity:

$$E_D = \frac{D_e}{D_m} = 1 + \frac{Sc^2 Wo^2 A^2}{8} \int\limits_{-1}^{1} \left(BG^* + B^*G\right) dY = \int\limits_{-1}^{1} = 1 + \frac{Sc^2 Wo^2 A^2}{8} S, \tag{19}$$

where the superscript * is the complex conjugate of the function. Here, the parameter S represents the interaction of the velocity and concentration profiles.

To assess how much the flow pulsation augments the mass transport in the channel, an analogy between mass and momentum transfer is implemented. It has been well reported that the velocity profiles exhibit the Hagen–Poiseuille shape at a low Wo. However, the parabolic shape is lost and the thinner boundary layer is shown, as Wo increases [8,10]. Thus, the augmented velocity gradient in the near-wall region brings forth a beneficial effect on mass transfer [9,10]. The time-averaged shear stress at the wall in the pulsating flow can be written as [9]

$$\overline{\sigma} = \frac{b\omega}{2\pi \overline{u}_{avg}} \int\limits_{0}^{2\pi/\omega} \left(\frac{\partial p}{\partial x}\right) \left(u_{avg}(t)\right) dt, \tag{20}$$

where $u_{avg}(t)$ denotes the cross-sectional average velocity at any time, and $\overline{u}_{avg}$ is the time-averaged bulk mean velocity, namely

$$u_{avg}(t) = \frac{1}{b} \int\limits_{0}^{b} u(y,t)\, dy, \quad \overline{u}_{avg} = \frac{\omega}{2\pi} \int\limits_{0}^{2\pi/\omega} u_{avg}(t) dt. \tag{21}$$

Substituting Eqs. (3) and (10) into Eq. (20), the time-averaged wall shear stress ratio of the pulsating flow to the steady flow can be drawn as follows:

$$E_\sigma = \frac{\overline{\sigma}}{\sigma_0} = 1 + \frac{2Wo^5 A^2}{3\sqrt{2}Re^2} \left[\frac{\sinh(\sqrt{2}Wo) - \sin(\sqrt{2}Wo)}{\cosh(\sqrt{2}Wo) + \cos(\sqrt{2}Wo)}\right]. \tag{22}$$

Through an analogy between mass and momentum transfer, the limiting current density enhancement factor which means the mass transport ratio of the pulsating flow to the steady flow can be expressed in terms of the time-averaged wall shear stress as follows [9,10]:

$$\frac{\bar{N}''}{\bar{N}_0''} = \left(\frac{\overline{\sigma}}{\sigma_0}\right)^{1/3} = \frac{j_L}{j_{0L}}. \tag{23}$$

It is clearly discernible from Eqs. (22) and (23) that the limiting current enhancement by flow pulsation is pronounced as the Womersley number Wo and the pulsating amplitude A increase. The flow pulsation effect, on the other hand, dwindles as the Reynolds number Re increases.

In the present mass transport analysis, the parameter ranges are $50 \le Re \le 150$, $0.1 \le Wo \le 10$, $1 \le A \le 7$ and $Sc = 0.765$, which cover the parameter ranges in the present fuel cell experiments. It should be noted that the tidal displacement should be smaller than the flow channel length to prevent direct convective mass transport in the axial direction [15,16], and this limitation can be expressed as $A < 16.67$ for the present pulsating cathode channel.

4. Results and discussion

4.1. Velocity measurement

To characterize the pulsating flow, it is useful to introduce the time-variant pulsating velocity $u = u_0 + \varepsilon \sin(\omega t)$. Here, u_0 represents the time-averaged inlet velocity which is related to the steady mean flow, and ε is the amplitude of the velocity fluctuation related to the flow oscillation. The tidal displacement represents the cross-stream-averaged maximum axial distance which the fluid elements travel during a one-half period of the pulsation [15]. The pulsating amplitude is half of the tidal displacement [16], namely
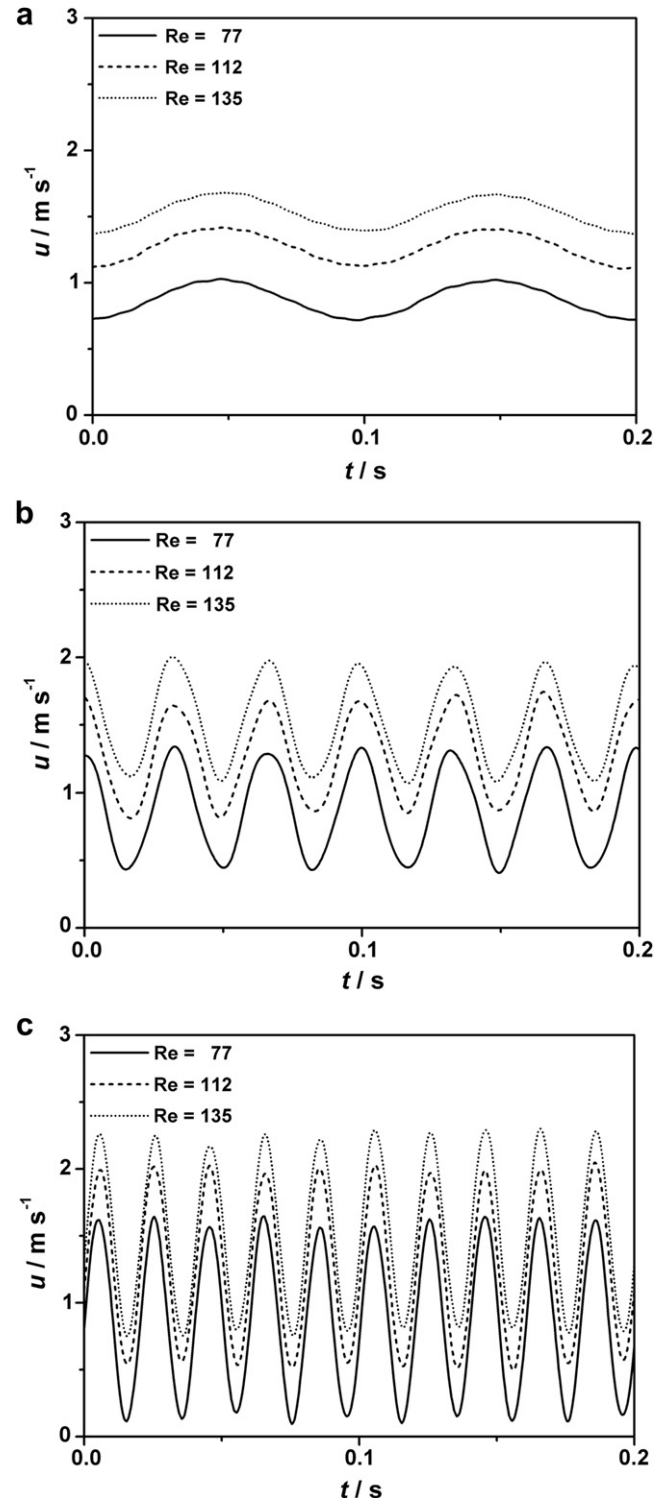

Fig. 4. Time-variant pulsating velocity u ($a = 0.0025$ m): (a) $f = 10$ Hz, (b) $f = 30$ Hz and (c) $f = 50$ Hz.

$$a = \frac{1}{2} \int_0^{\pi/\omega} \varepsilon \sin(\omega t) \mathrm{d}t = \varepsilon/\omega . \tag{24}$$

The Womersley number $Wo = b(\omega/\nu)^{1/2}$ and the well-known Reynolds number $Re = 2u_{0\text{avg}}b/\nu$ can be calculated from the measured velocity. Here, a polynomial approximation for the maximum-to-average velocity ratio in laminar flow through a rectangular duct is adopted to predict the cross-stream averaged velocity $u_{0\text{avg}}$ by using the measured center-line velocity [17],

$$\frac{u_0}{u_{0\text{avg}}} = \frac{3}{2}\Big(1 + 0.546688\text{Ar} + 1.552013\text{Ar}^2 - 4.059427\text{Ar}^3$$
$$+ 3.214927\text{Ar}^4 - 0.857313\text{Ar}^5\Big). \tag{25}$$

The measured time-variant pulsating velocities at the mid portion of the cathode channel inlet are displayed in Fig. 4 when the pulsating amplitude is fixed at $a = 0.0025$ m. The time-averaged inlet velocity u_0 is varied from 0.87 m s^{-1} to 1.53 m s^{-1} and the amplitude of pulsating velocity ε ranges from 0.16 m s^{-1} to 0.78 m s^{-1} to fix the pulsating amplitude for all the flow conditions tested. The frequency spectrum for the velocity fluctuation at $Re = 112$ discloses that the present acoustic excitation can provide quite accurate sinusoidal flow pulsations at a specific forcing frequency f and pulsating amplitude a, see Fig. 5.

4.2. Fuel cell performance

The polarization and corresponding power curves for the NP50 PEM stack according to the Womersley number Wo are demonstrated in Fig. 6. In order to scrutinize the effect of Wo, the pulsating amplitude is maintained at $a = 0.0025$ m and the inlet gas temperatures at the anode and the cathode are fixed at 30 °C and 35 °C, respectively. Also, the relative humidities at the anode and cathode inlet are set at 70% and 80%, respectively. Such an experimental condition may be unrealistic comparing to the actual air and fuel supply devices in PEM fuel cell systems. However, the impact of the flow parameters as well as the oscillating frequency on the performance of the PEM fuel cell can be clearly and quantitatively identified by adopting the present experimental setup. The Reynolds number of cathode flow is changed in the range of 77 (Fig. 6a) to 135 (Fig. 6c) at a constant hydrogen flow rate of 2 lpm and a stack temperature of 50 °C.
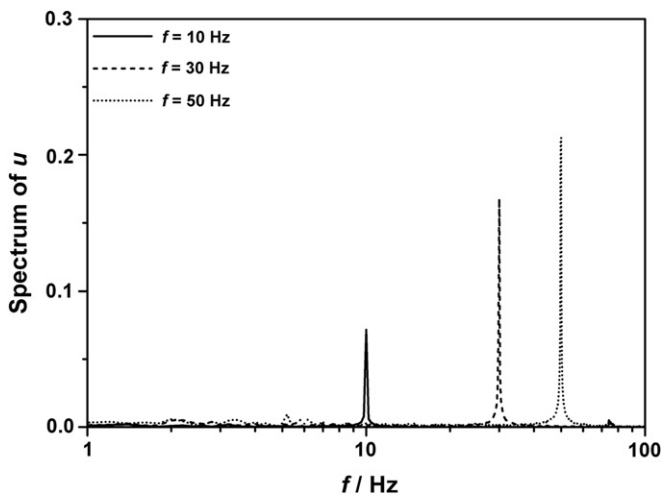
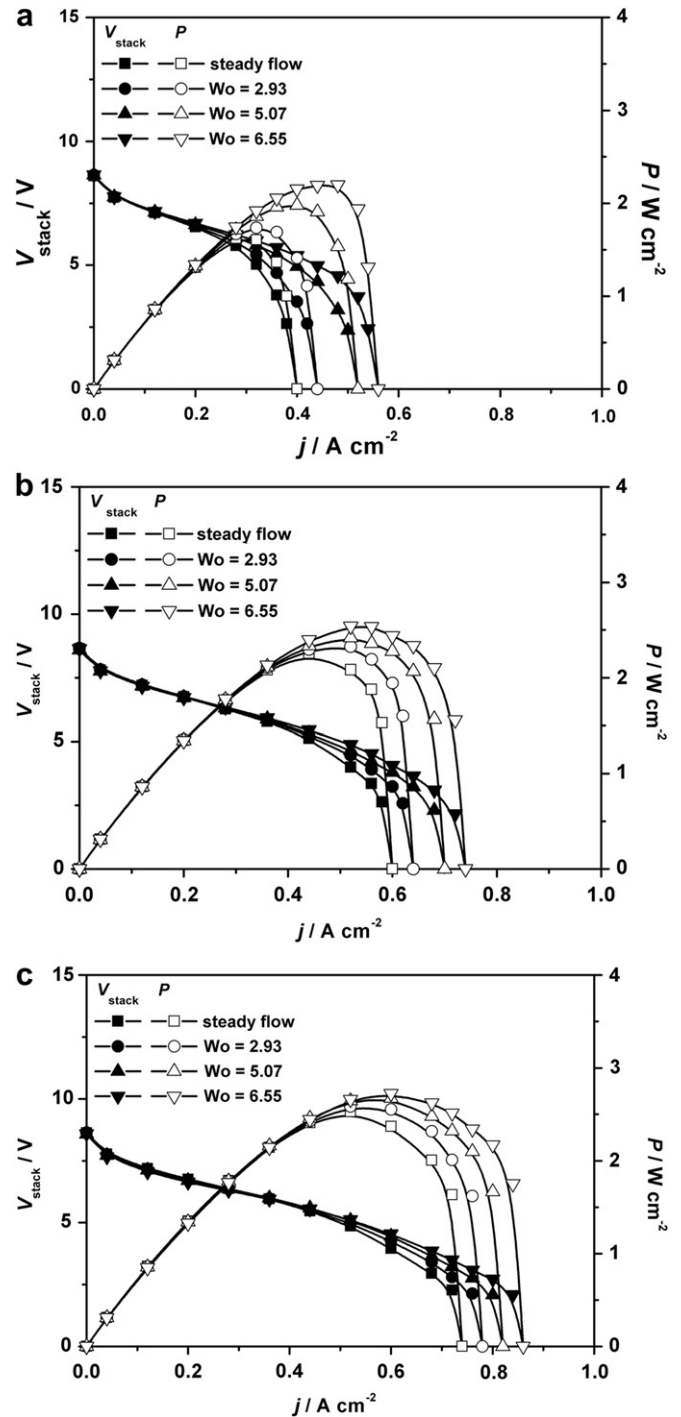**Fig. 5.** Power spectrum of the forcing frequency ($Re = 112$).

Fig. 6. Polarization and power curves according to the Womersley number: (a) $Re = 77$, (b) $Re = 112$ and (c) $Re = 135$.

It is evident that the enhancement of V_{stack} by the flow pulsation is negligible at low current loadings. As the Womersley number increases, however, the cathode flow pulsation significantly enhances the fuel cell performance at the concentration loss region. The concentration loss in the polarization behavior is dramatically reduced by the cathode flow pulsation, while the activation and ohmic losses remain unchanged. The limiting current density j_L increases with Wo due to the enhanced dispersion of reactant in the cathode channels. Accordingly, the maximum power density is also augmented. As shown in Fig. 6a, the limiting current density and

the maximum power density for the steady flow at $Re = 77$ is 0.4 A cm^{-2} and 1.62 W cm^{-2}, respectively. As the oscillating flow is added at $Wo = 6.55$ and $a = 0.0025$ m, however, they are dramatically augmented up to 0.56 A cm^{-2} and 2.20 W cm^{-2}, respectively. The effect of cathode flow pulsation at $Re = 112$ is given in Fig. 6b. The limiting current and maximum power densities are 0.60 A cm^{-2} and 2.26 W cm^{-2} for a steady non-pulsating flow, respectively. They are increased up to 0.74 A cm^{-2} and 2.54 W cm^{-2} by the cathode flow pulsation of $Wo = 6.55$, respectively. For $Re = 135$, the limiting current densities are 0.74 A cm^{-2} and 0.86 A cm^{-2} for steady flow and pulsating flow of $Wo = 6.55$ operations, respectively, see Fig. 6c. The maximum power density is augmented from 2.53 W cm^{-2} to 2.72 W cm^{-2}. It is clearly discernible that the enhancement of the limiting current density and the maximum power density dwindles away as Re increases.

To assess the effect of the cathode flow pulsation on the overall fuel cell performance, it is convenient to introduce the enhancement factors in the limiting current density and the maximum power density as follows:

$$E_j = j_L/j_{0L}, \tag{26}$$

$$E_P = P_{max}/P_{0max}, \tag{27}$$

where the subscript 0 denotes the steady non-pulsating flow. Thus, the enhancement factor represents the ratio of the pulsating cathode flow to the steady flow. Fig. 7 illustrates the variation of the limiting current density enhancement factor E_j and the maximum power density enhancement factor E_P. The enhancement factors increase as the cathode inlet flow oscillates at higher Wo. The pulsating cathode flow of $Wo = 6.55$ gives rise to 40.0%, 23.3% and 16.2% increments in the limiting current density when the Reynolds numbers are 77, 112 and 135, respectively, see Fig. 7a. As highlighted in Fig. 7b, it also provides 35.5%, 12.5% and 7.9% higher maximum power density compared to the steady non-pulsating flow for $Re = 77$, 112 and 135, respectively. As expected, the enhancement factors are more pronounced as Re decreases. These results imply that the flow pulsation is more effective at low Re. For high Re, the oxygen concentration in the cathode channel is sufficient for the full electrochemical reaction so that the enhancement by the flow pulsation is meager. It is anticipated that the trend of enhanced performance by the cathode flow pulsation can be also obtained in actual PEM fuel cell systems by adopting an appropriate pulse generating device.

4.3. Fuel cell efficiency

The fuel cell efficiency based on the higher heating value is expressed by [3]:

$$\eta = \mu \frac{V_{cell}}{1.48}, \tag{28}$$

where, V_{cell} is the average cell voltage and μ is the fuel utilization coefficient defined as the fuel ratio of the consumption in a cell to the supply into a cell. The efficiency of a fuel cell can be estimated from the simple measurement of V_{cell} when a good estimate for μ is 0.95 [3].

The fuel cell efficiency η as a function of power density P at a pulsating amplitude of $a = 0.0025$ m is presented in Fig. 8. Fig. 8a shows that a maximum power density of 1.62 W cm^{-2} is obtained at the efficiency of 37.2% for the steady non-pulsating flow of $Re = 77$. The maximum power density increases up to 1.74 W cm^{-2}, 1.98 W cm^{-2} and 2.20 W cm^{-2} for the Womersley number of 2.93, 5.07 and 6.55, respectively. The corresponding fuel cell efficiencies are 34.8%, 31.7% and 29.4%, respectively. Therefore, the substantially
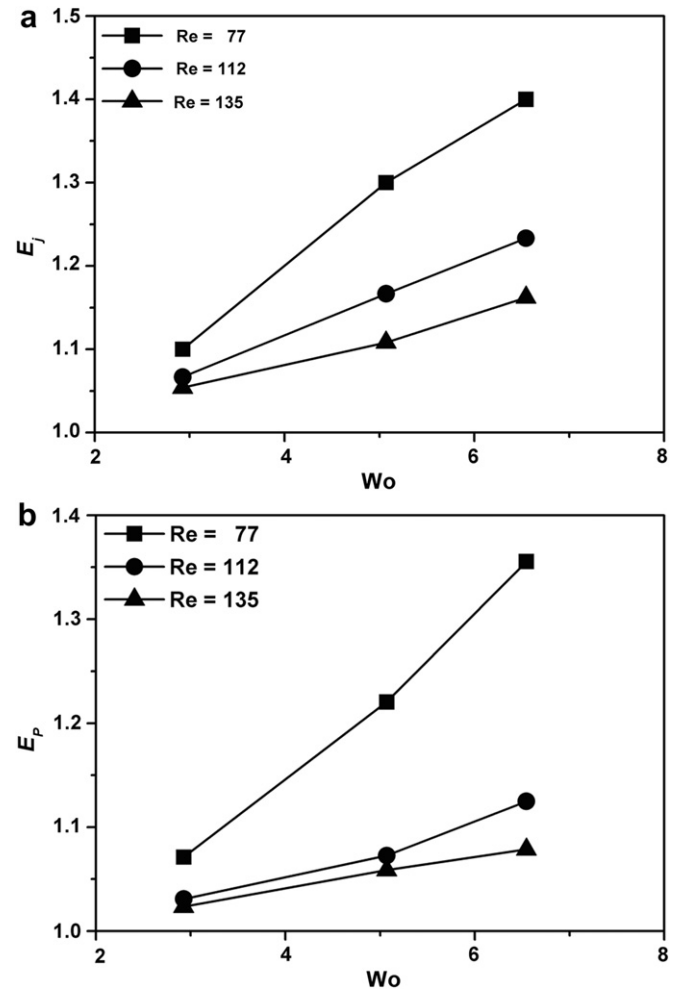

Fig. 7. Enhancement factors versus the Womersley number: (a) limiting current density and (b) maximum power density.

enhanced maximum power density with Wo can be achieved at a slightly reduced efficiency by adopting the cathode flow pulsation. Even at the identical efficiency, the cathode flow pulsation yields the prominent enhancement of power density. It should be noticed in Fig. 8b and c that the maximum power density enhancement with Wo dwindles as the Reynolds number increases. Hence, it is clear that the cathode flow pulsation is more effective at low Re.

4.4. Mass transport in a pulsating cathode flow channel

The dispersion coefficient ratio can be estimated from the experimental results of the PEM fuel cell stack with a cathode pulsating flow. Assuming the time-averaged axial concentration gradient is constant, the time-averaged axial mass flux can be expressed as

$$\dot{N}_0'' = u_{0avg}(c_{0in} - c_{0out}) - D_m \frac{c_{0out} - c_{0in}}{l} = \frac{j_0}{nF}, \tag{29}$$

$$\bar{\dot{N}}'' = \bar{u}_{avg}(\bar{c}_{in} - \bar{c}_{out}) - D_e \frac{\bar{c}_{out} - \bar{c}_{in}}{l} = \frac{j}{nF}, \tag{30}$$

for the steady non-pulsating flow and the pulsating flow, respectively. Here, l is the flow channel length occupied by the MEA, n is number of electrons transferred in the reaction, F is Faraday's constant ($F = 96485.34$ C mol^{-1}), and the bars designate the time-averaged value. Supposing that all the oxygen in the cathode
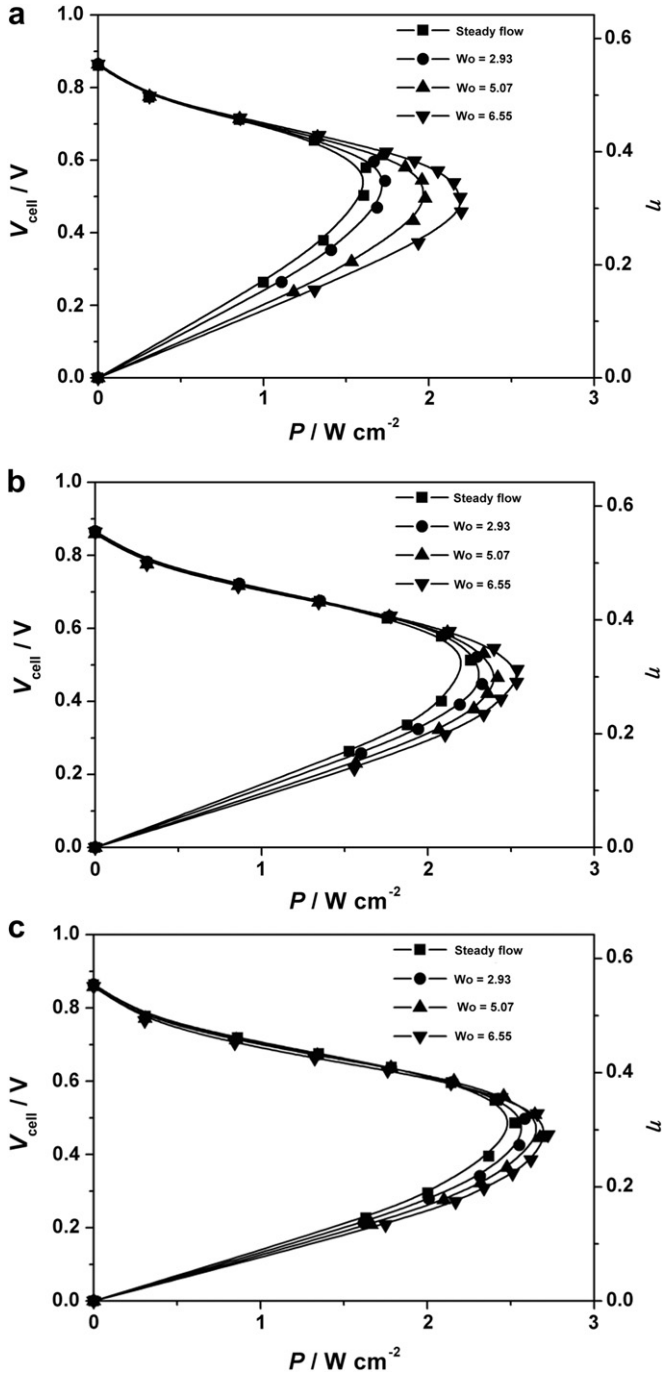
Fig. 8. Fuel cell efficiency according to the Womersley number: (a) $Re = 77$, (b) $Re = 112$ and (c) $Re = 135$.

Table 1
Geometrical parameters and physical properties.

| Quantity	Value	Reference
Cathode channel length occupied by MEA, l	0.05 m	Present experiment
Cathode channel width, $W = 2b$	0.003 m	
Pulsating amplitude, a	0.0025 m	
Dimensionless pulsating amplitude, $A = a/b$	1.65	
Cathode pressure, p	1 atm	
Cathode channel temperature, T	35 °C	
Relative humidity of inlet air, RH	80%	
Number of mole electrons transferred in the cathode reaction, n	4	[1−3]
Oxygen diffusivity in gas at standard condition, D_{st}	0.18×10^{-4} m^2 s^{-1}	[2]
Oxygen molecular diffusivity, $D_m = D_{st}(T/T_{st})^{3/2}(p_{st}/p)$	2.157×10^{-5} m^2 s^{-1}	[2,7]
Oxygen concentration at the channel inlet, c_{0in}	7.945 mol m^{-3}	[18]
Kinematic viscosity of inlet air, ν	1.650×10^{-5} m^2 s^{-1}	[18]
Schmidt number, $Sc = \nu/D_m$	0.765	[2,7,18]
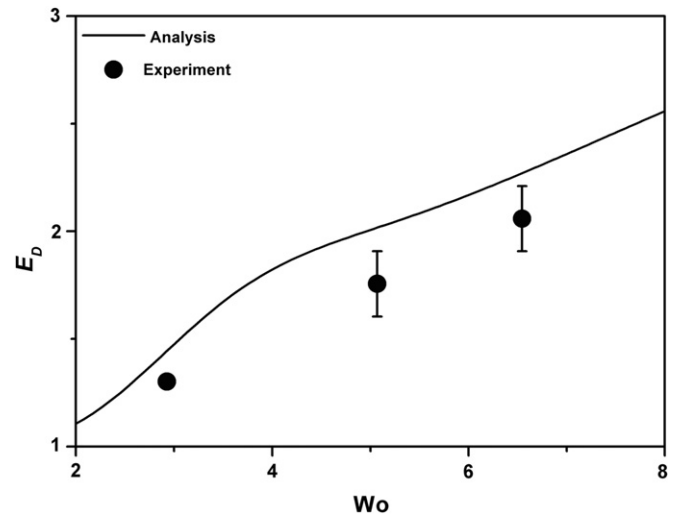
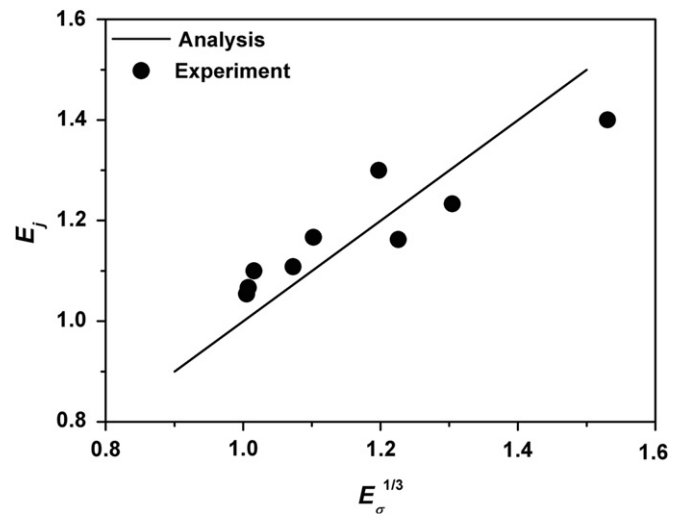**Fig. 9.** Dispersion coefficient ratio ($A = 1.65$ and $Sc = 0.765$).

Fig. 10. Relation between the limiting current density and the time-averaged wall shear stress.

channel is entirely consumed by the electrochemical reaction in the mass transport limit situation, the time-averaged bulk concentration at the channel outlet can be assumed to be zero [1,2]. Subtracting Eq. (30) from Eq. (29) gives the dispersion coefficient ratio with the equalities of $u_{0avg} = \overline{u}_{avg}$ and $c_{0in} = \overline{c}_{in}$:

$$\frac{D_e}{D_m} = 1 + \frac{l}{c_{0in}} \frac{j_L - j_{0L}}{nFD_m}. \tag{31}$$

The geometrical parameter and the physical properties are listed in Table 1. Here, the oxygen molecular diffusivity D_m is a function of temperature and pressure [2,7].

In Fig. 9, the dispersion coefficient ratios evaluated from the fuel cell experiments [Eq. (31)] are compared with the theoretical analysis [Eq. (19)] when the dimensionless pulsating amplitude and the Schmidt number are $A = 1.65$ and $Sc = 0.765$, respectively. The dispersion coefficient ratio increases with the increase of Wo.

The experimental results show that the effect of Wo is in well accordance with the theoretical analysis. Some discrepancy is due to the fact that the present analysis adopts the simple constant mass flux boundary condition, excludes the reaction site where the complicated electrochemical reaction occurs, and disregards the
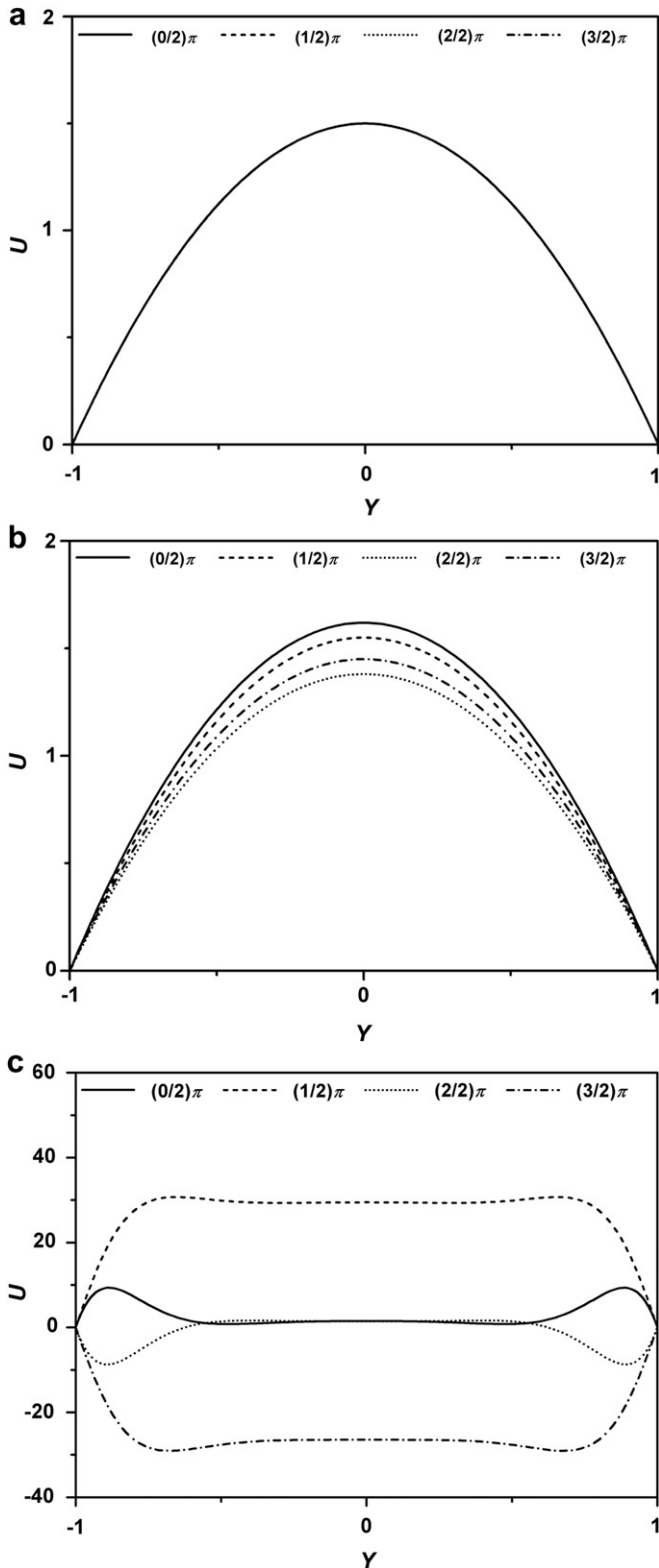

Fig. 11. Effect of the Womersley number on the time-variant velocity profile ($A = 7$ and $Re = 50$): (a) $Wo = 0.1$, (b) $Wo = 1$ and (c) $Wo = 10$.
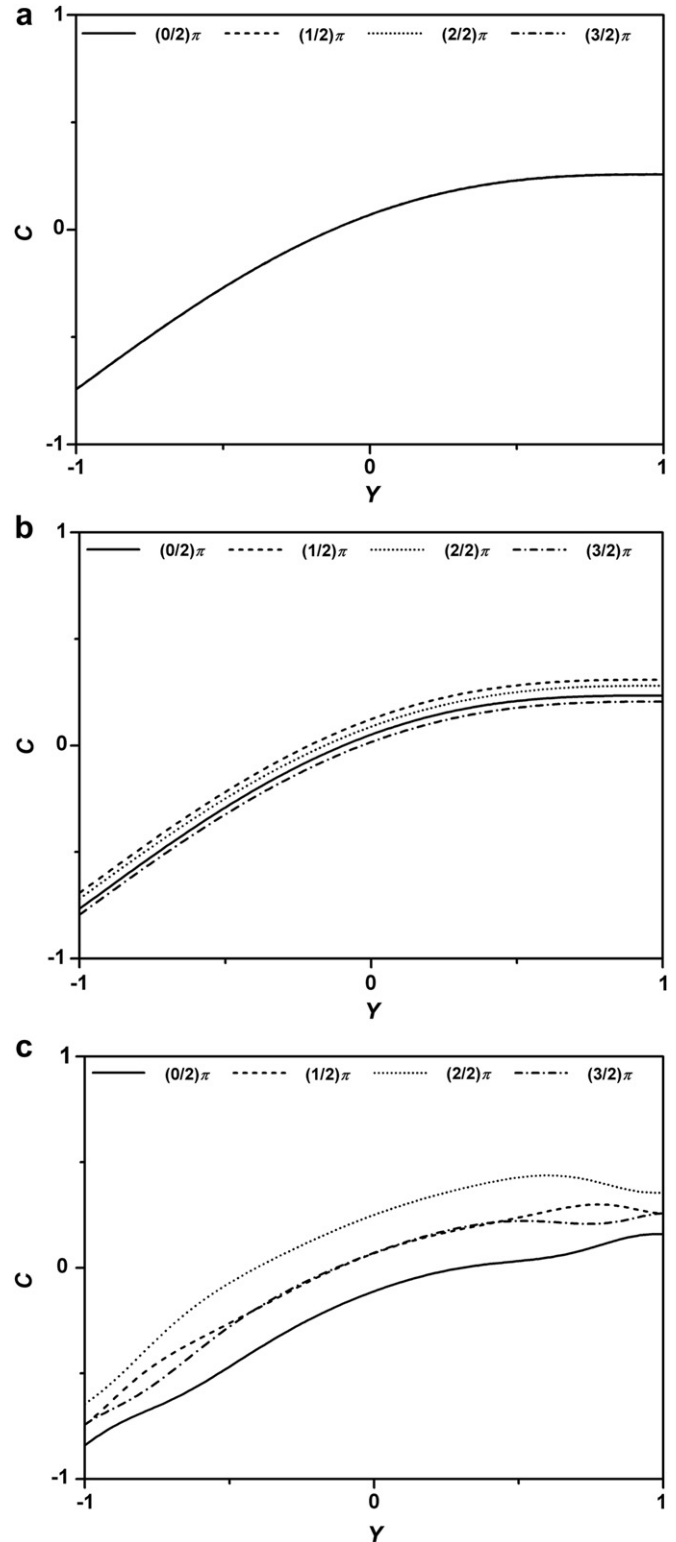

Fig. 12. Effect of the Womersley number on the time-variant concentration profile at the channel inlet ($A = 7$ and $Re = 50$): (a) $Wo = 0.1$, (b) $Wo = 1$ and (c) $Wo = 10$.

3D effect of the diffusive transport into the catalyst layer, to name a few.

In Fig. 10, the experimental values of the limiting current density enhancement factor E_j are plotted against the time-averaged wall shear stress ratio to the power of one-third $E_\sigma^{1/3}$ evaluated from Eq. (22). Also, the theoretical prediction given by Eq. (23) is presented as a solid line. The experimental results are shown to be consistent with the theoretical ones within 8.6% deviation. It is evident that flow pulsation contributes to increase the limiting current density.

The analytical velocity profiles according to Wo during a single cycle of the flow pulsation are displayed in Fig. 11. As the Womersley number Wo increases from 0.1 to 10 at $A = 7$ and $Re = 50$, the flow field is substantially affected by the flow pulsation [8,13]. The velocity magnitude is augmented and the boundary layer becomes thinner with the increase of Wo. The velocity profile at the core becomes flat.

Fig. 12 illustrates the effect of flow pulsation on the concentration profiles at the channel inlet ($X = 0$) when the dimensionless pulsating amplitude and the Reynolds number are $A = 7$ and $Re = 50$, respectively. The left side wall shows the lowest oxygen concentration because the oxygen gas is being consumed by the electrochemical reaction, as depicted in Fig. 3. In the same manner as in the velocity profile, the effect of flow pulsation on the concentration field is meager when Wo is low. As Wo increases,

however, the concentration profile begins to oscillate periodically because the pulsating velocity directly affects the concentration field, see Eq. (2). It is discernible from Fig. 12c that the concentration intensively fluctuates in the core region where the velocity oscillating magnitude is high. Also, the phase lag with respect to the velocity fluctuation is shown, which plays a key role in mass transport enhancement by the interaction of the velocity and concentration profiles [14,15].
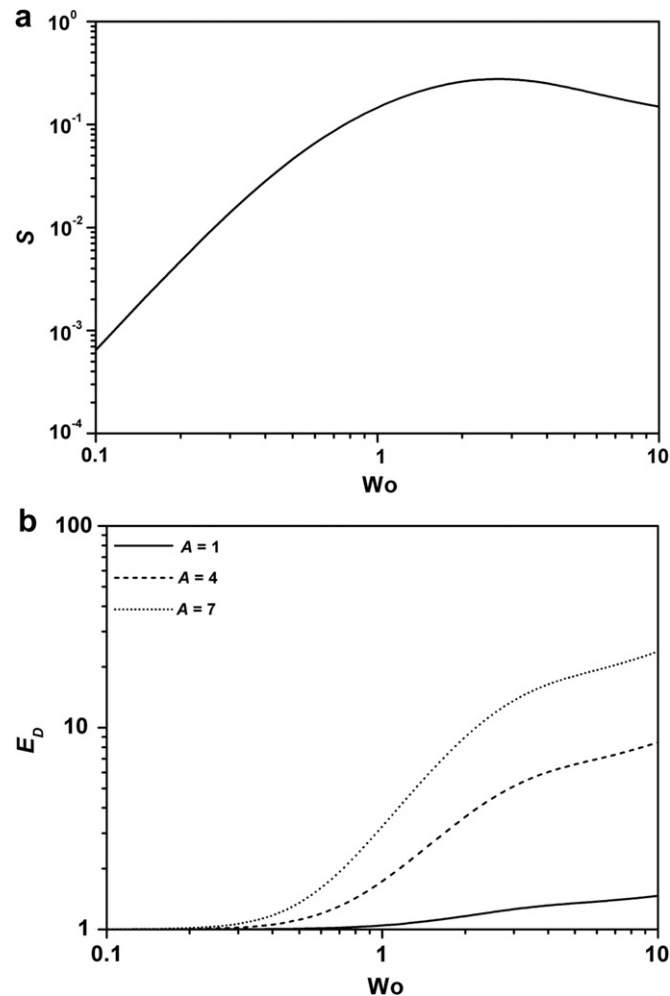

Fig. 13. Effective time-averaged dispersion coefficient: (a) interaction function between the velocity and concentration profiles S and (b) dispersion coefficient ratio E_D.
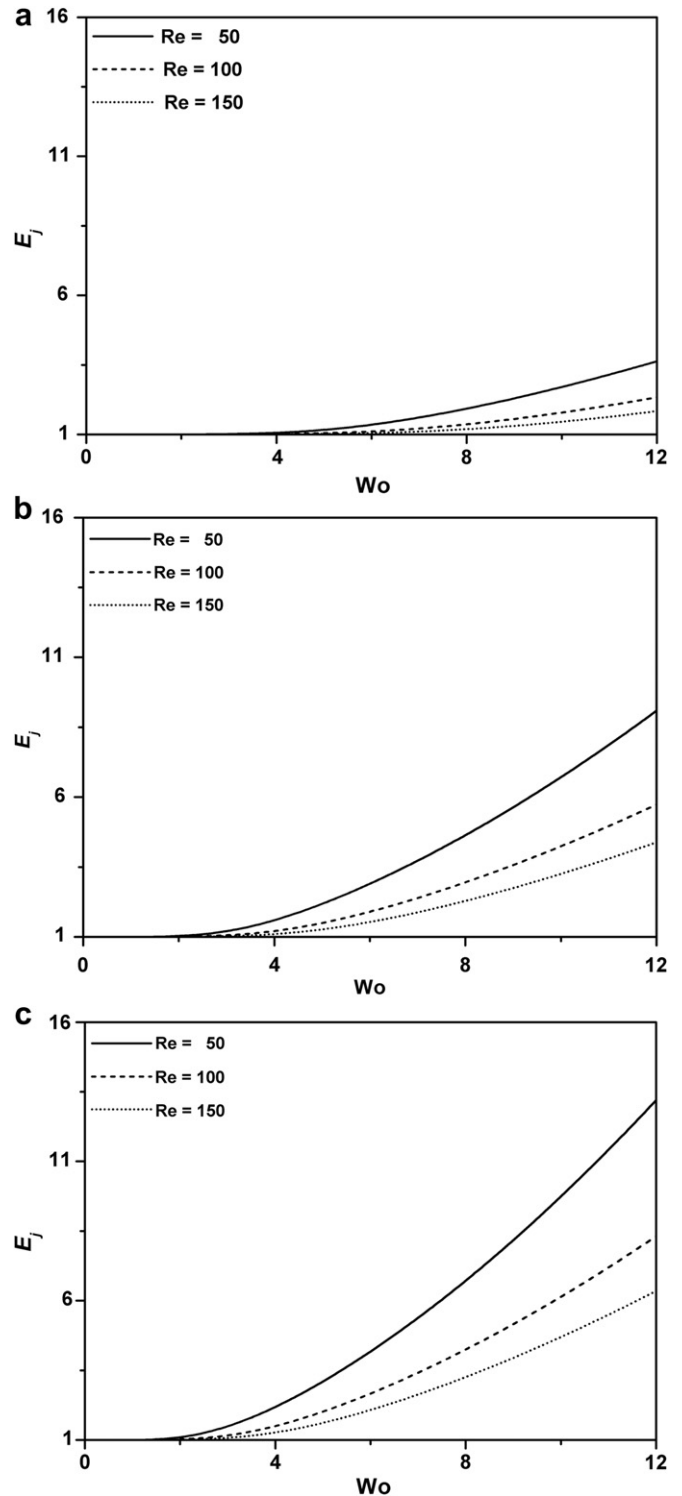

Fig. 14. Limiting current density enhancement factor: (a) $A = 1$, (b) $A = 4$ and (c) $A = 7$.

The effective time-averaged dispersion coefficient is elucidated from Fig. 13 by plotting the parameter S which represents the interaction of the velocity and concentration profiles. The interaction function S increases to a maximum and gradually decreases beyond $Wo \sim 3$ as Wo increases, see Fig. 13a. As shown in Fig. 13b, therefore, the increasing rate of the dispersion coefficient ratio E_D slows in the region of $Wo = 1$ because the dispersion coefficient enhancement is proportional to the product of the Wo^2 and S, see Eq. (19). Physically, the fluid never has enough time for diffusion from the high concentration core region to the low concentration near-wall region or vice versa under fast oscillation, i.e. high Wo, which means the molecular diffusion time scale is much larger than the one-half period of the oscillation [15,19]. The increase of the dimensionless pulsating amplitude A results in a substantial enhancement of the dispersion coefficient due to the intensified pulsating effect.

Fig. 14 exhibits the limiting current density enhancement factor E_j calculated from Eqs. (22) and (23). The limiting current density enhancement factor is almost unity which is equal to the steady flow value at low Womersley numbers. As Wo increases, however, it is steeply increased by the enhanced axial dispersion in the cathode flow channel. The enhancement of the limiting current density is more pronounced at higher A because of the intensified pulsating effect. Also, it is discernible that the enhancement factor dwindles as Re increases. For high Re, the mass transport by the steady forced convection in the channel can be enough for the electrochemical reaction even in the absence of the flow pulsation.

5. Conclusions

The effect of the pulsating cathode flow on the overall performance of a PEM fuel cell has been investigated. The polarization and corresponding power curves are experimentally obtained to investigate the impact of the Womersley number and the Reynolds number on the performance of a 10-cell PEM fuel cell stack. As the pulsating component is delivered only to the cathode mainstream flow, the performance of the PEM fuel cell stack in the concentration loss region is prominently increased due to the enhanced axial dispersion. The increased limiting current density is obtained at higher Wo. The cathode flow pulsation at $Wo = 6.55$ yields 40.0%, 23.3% and 16.2% augmented limiting current densities compared to the steady non-pulsating flow for $Re = 77, 112$ and 135, respectively. Accordingly, the maximum power density increases with Wo at a slightly reduced fuel cell efficiency. The maximum power density shows 35.5%, 12.5% and 7.9% increments, respectively. Enhancement of the overall performance is more pronounced at low Re. Consequently, the flow pulsation extends the mass transport limit in the cathode channel, similarly the increase of steady flow rate by adopting high capacity blowers or compressors.

In addition, a theoretical mass transport analysis in the pulsating cathode flow channel has been implemented to verify the experimental results. The cathode flow pulsation increases the oxygen axial dispersion in the cathode channel so that the limiting current density increases with the Womersley number and the pulsating amplitude. As the Reynolds number increases, however, the enhancement of the limiting current density dwindles due to the reduced pulsating effect. This theoretical mass transport analysis shows that the effect of the relevant parameters is in well accordance with the 10-cell PEM fuel cell stack experiments.

References

[1] R. O'Hayre, S.W. Cha, W. Colella, F.B. Prinz, Fuel cell fundamentals, John Wiley & Sons, New York, 2006.
[2] X. Li, Principles of fuel cells, Taylor & Francis Group, New York, 2006.
[3] J. Larminie, A. Dicks, in: Fuel cell systems explained, second ed. John Wiley & Sons, West Sussex, England, 2003.
[4] Y. Wang, K.S. Chen, J. Mishler, S.C. Cho, X.C. Adroher, Appl. Energy 88 (2011) 981–1007.
[5] Y.H. Kim, H.S. Han, S.Y. Kim, G.H. Rhee, J. Power Sources 185 (2008) 112–117.
[6] S.Y. Kim, W.N. Kim, J. Power Sources 166 (2007) 430–434.
[7] R.B. Bird, W.E. Stewart, E.N. Lightfoot, in: Transport phenomena, second ed. John Wiley & Sons, New York, 2002.
[8] C. Loundon, A. Tordesillas, J. Theoret. Biol. 191 (1998) 63–78.
[9] J.H. Krasuk, J.M. Smith, Chem. Eng. Sci. 18 (1963) 591–598.
[10] V. Perez-Herranz, J. Garcia-Anton, J.L. Guinon, Chem. Eng. Sci. 52 (1997) 843–851.
[11] T. Moschandreou, M. Zamir, Int. J. Heat Mass Transfer 40 (1997) 2461–2466.
[12] J.-C. Yu, Z.-X. Li, T.S. Zhao, Int. J. Heat Mass Transfer 47 (2004) 5297–5301.
[13] H.N. Hemida, M.N. Sabry, A. Abdel-Rahim, H. Mansour, Int. J. Heat Mass Transfer 45 (2002) 1767–1780.
[14] E.J. Watson, J. Fluid Mech. 133 (1983) 233–244.
[15] U.H. Kurzweg, J. Fluid Mech. 156 (1985) 291–300.
[16] M.J. Jaeger, U.H. Kurzweg, Phys. Fluids 26 (1983) 1380–1382.
[17] M. Spiga, G.L. Morini, Int. Comm. Heat Mass Transfer 21 (1994) 469–475.
[18] R.H. Perry, D.W. Green, J.O. Maloney, Perry's chemical engineers' handbook, seventh ed. McGraw-Hill, New York, 1997.
[19] U.H. Kurzweg, G. Howell, M.J. Jaeger, Phys. Fluids 27 (1984) 1046–1048.